Numerical Heat Transfer, Part A, 61: 1–17, 2012

ISSN: 1040-7782 print/1521-0634 online
DOI: 10.1080/10407782.2012.631384

Taylor & Francis
Taylor & Francis Group

TEMPERATURE DISTRIBUTION IN A COUNTERFLOW MOVING BED UNDER A THERMAL NONEQUILIBRIUM CONDITION

Ana C. Pivem and Marcelo J. S. de Lemos
Departamento de Energia – IEME, Instituto Tecnológico de Aeronáutica — ITA, Sao Paulo, Brazil

This work investigates the influence of physical properties on heat transfer between solid and fluid phases in a moving porous bed, in which the working fluid flows in the opposite direction with respect to the permeable medium. A two-energy equation model is applied in addition to a macroscopic mechanical model for laminar flow. Transport equations are discretized using the control-volume method and the system of algebraic equations is relaxed via the SIMPLE algorithm. The effects on inter-phase heat transfer due to variation of Reynolds number, solid-to-fluid velocity ratio, solid-to-fluid thermal capacity ratio, permeability, porosity, and solid-to-fluid thermal conductivity ratio are analyzed. Results for a counterflow moving bed indicate that motion of solid material, contrary to the direction of the fluid, enhances heat transfer between phases. The same effect was observed for smaller Darcy numbers and porosity, as well as for higher solid-to-fluid thermal capacity and thermal conductivity ratios.

INTRODUCTION

Exchange of thermal energy by means of counterflow heat transfer equipment is often encountered in a number of engineering processes. Two streams separated by a solid plate and flowing in opposite but aligned directions constitute the most common configuration of counterflow heat exchangers. Examples are certain types of cooling towers, boilers, condensers, evaporators, and fluidized bed, among others [1–3]. Configurations where both fluid streams are not aligned but rather perpendicular to each other, are called "cross-flow" heat exchangers as opposed to the counterflow arrangement investigated here [4].

Further study in the literature is the work by Ansari and Mortazavi [5], who conducted simulation of dynamical response of a countercurrent heat exchanger to inlet temperature or mass flow rate change. Kranc [6] presented a method to estimate the performance of a counterflow cooling tower packed with a regular fill. Ay et al. [7] presented a numerical model to calculate performance information about

Received 11 May 2011; accepted 26 September 2011.
The authors are thankful to CNPq, Brazil for their financial support during the course of this research.
Address correspondence to Marcelo J. S. de Lemos, Departamento de Energia – IEME, Instituto Tecnológico de Aeronáutica — ITA, 12228-900, São José dos campos, São Paulo, Brazil. E-mail: delemos@ita.br

NOMENCLATURE

c_F	Forchheimer coefficient
c_p	specific heat
D	particle diameter
D	deformation rate tensor, $\mathbf{D} = [\nabla \mathbf{u} + (\nabla \mathbf{u})^T]/2$
H	Distance between channel walls
K	Permeability
L	Channel length
p	Thermodynamic pressure
$\langle p \rangle^i$	Intrinsic (fluid) average of pressure p
Re	Reynolds number, $Re_H = \rho u_{D_{in}} 2H/\mu$, $Re_D = \rho \lvert \mathbf{u}_{rel} \rvert D/\mu$
$\langle T_f \rangle$	Fluid temperature
$\langle T_s \rangle$	Solid temperature
$\mathbf{u}$	Microscopic velocity vector
$\langle \mathbf{u} \rangle^i$	Intrinsic (fluid) average of $\mathbf{u}$
$\mathbf{u}_D$	Darcy velocity vector, $\mathbf{u}_D = \phi \langle \mathbf{u} \rangle^i$
$\mathbf{u}_S$	Total-volume-based solid velocity vector
u_D	x-component of $\mathbf{u}_D$
u_S	x-component of $\mathbf{u}_S$
$\mathbf{u}_{rel}$	Relative velocity based on total volume
$\mathbf{K}_{eff}$	Effective thermal dispersion tensor
k_s/k_f	Thermal conductivity ratio
A_i	Interfacial area
a_i	Interfacial area per unit volume
h_i	Interfacial heat transfer coefficient
x, y	Cartesian coordinates

Greek

μ	Fluid dynamic viscosity
ρ	Density
φ	General variable
γ	Phase identifier
ϕ	Porosity

Subscript

s,f	s=solid, *f*=fluid
in, out	in=inlet, *out*=outlet

direct-contact heat transfer between a rising dispersed refrigerant and a counterflow continuous fluid. Souid and Bontemps [8] studied countercurrent gas-liquid flow in narrow rectangular channels simulated by plain and perforated fins. The main advantage of counterflow over concurrent flow is that the outlet temperature of the cold phase can be higher than the outlet temperature of the hot phase; whereas in a concurrent flow configuration, this temperature reaches, at the most, the equilibrium temperature of phases.

A moving porous bed fully saturated by a cold fluid, which moves in the opposite direction of a hot permeable bed, can also be seen as a counterflow heat exchanger and such a configuration can be found in a number of materials and energy production systems. Rajan et al. [9] showed the effect of solid loading ratio and particle size in a simulation of a countercurrent gas–solid heat exchanger. Valipour et al. [10] described a model to predict flow in a cylindrical reactor in which pellets of iron ore went through a gas mixture. Henda and Falcioni [11] described the thermal performance of a pre-heater that consists of a moving bed of pellets of nickel in concurrent flow with a gas, using both one and two equations energy models.

Biomass gasification for energy production may also consider systems having a moving porous bed. Examples are given by Ryu et al. [12], Boman et al. [13], and Shimizu et al. [14], who presented mathematical models of the gasification of a system using a moving bed in the burning of biomass. Kayal and Chakravarty [15], Rogel et al. (2006) [16] and Nussbaumer et al. (2003) [17] investigated technologies to cope with the problem of pollutant emission during of combustion and co-combustion of biomass.

In an accompanying paper [18], concurrent or parallel flow in a moving porous bed was investigated using a two-equation approach for handling thermal

non-equilibrium [19] along with a model for treating the movement of the solid phase [20]. Therein, only parallel flow cases were investigated, or say, the movement of the solid porous matrix was always in the same direction of that of the working fluid.

The objective of the present contribution is to extend the parallel-flow analysis of [18] to investigate now counterflow cases. Here, the solid material flows steadily in opposite direction of that of the fluid. By that, a number of engineering flows of practical relevance can be evaluated such as flow in biomass gasifiers and in equipment for advanced materials production.

MACROSCOPIC MODEL FOR FLOW EQUATIONS

For a moving bed, only cases where the solid phase velocity is kept constant will be considered, or say, we consider here a moving rigid bed that crosses a fixed control volume in addition to a flowing fluid, which is not necessarily moving with a velocity aligned with the solid phase velocity. Figure 1*a* identifies possible configurations for the relative movement between phases. In a parallel or concurrent arrangement, as the positive ratio u_S/u_D increases, the relative velocity is reduced and, consequently, relative friction between phases will decrease. On the other hand,

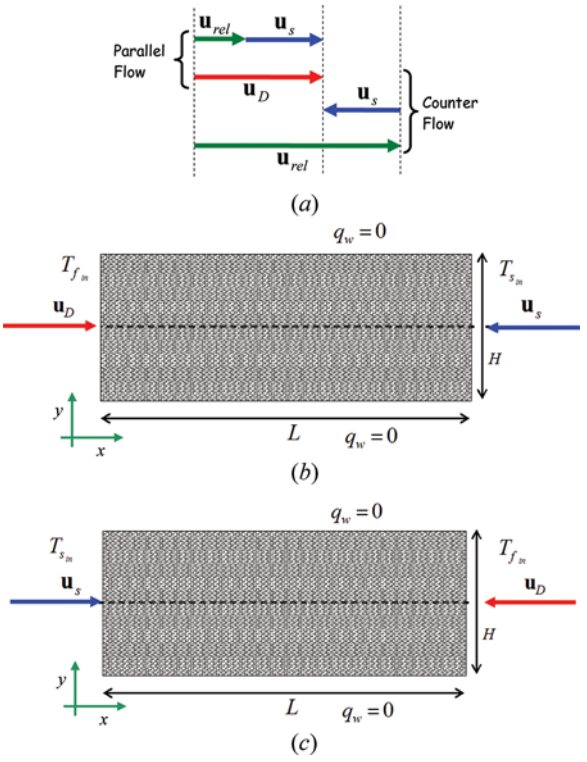

Figure 1. Porous bed reactor with a moving solid matrix. (*a*) Flow configurations, (*b*) counterflow with fluid moving west to east, and (*c*) counterflow with fluid moving east to west (color figure available online).

for $u_S/u_D < 0$ as in counterflow cases, the increase in the relative velocity will impact on the transport of momentum and heat between the fluid and the solid substrate. The models below intend to reflect such reasoning.

Further, as the equations to follow are fully available in the open literature, their derivation are not repeated here and, to the interested reader, reference [21] is suggested for further modeling details. Also, before transport equations for the moving bed cases are presented, the mathematical model for a standard fixed bed is shown for the sake of completeness.

FIXED BED

A macroscopic form of the governing equations is obtained by taking the volumetric average of the entire equation set. In this development, the porous medium is considered to be rigid, fixed, isotropic and saturated by the incompressible fluid. Also, no buoyancy effects are considered here. For a discussion on buoyant flows modeling in heterogeneous systems, see reference [22].

As mentioned, derivation of this equation set is already available in the literature [21], so details are not repeated here. Nevertheless, for the sake of completeness, the final laminar incompressible form of the equations is presented.

Continuity

$$\nabla \cdot \mathbf{u}_D = 0 \tag{1}$$

Momentum

$$\rho\left[\frac{\partial \mathbf{u}_D}{\partial t} + \nabla \cdot \left(\frac{\mathbf{u}_D \mathbf{u}_D}{\phi}\right)\right] = -\nabla(\phi\langle\bar{p}\rangle^i) + \mu\nabla^2\mathbf{u}_D - \left[\frac{\mu\phi}{K}\mathbf{u}_D + \frac{c_F\phi\rho|\mathbf{u}_D|\mathbf{u}_D}{\sqrt{K}}\right] \tag{2}$$

where the last two terms in Eq. (2) represent the Darcy and Forchheimer contributions.

MOVING BED

The steps below show some basic definitions prior to presenting a proposal for a set of transport equations for analyzing systems schematically, shown in Figure 1*a*. Here, the moving medium is supposed to be isotropic.

A general form for a volume-average of any property φ, distributed within a phase γ that occupy volume ΔV_γ, can be written as [23, 24]

$$\langle\varphi\rangle^\gamma = \frac{1}{\Delta V_\gamma}\int_{\Delta V\gamma} \varphi dV_\gamma \tag{3}$$

In the general case, the volume ratio occupied by phase γ will be $\phi^\gamma = \Delta V_\gamma/\Delta V$.

If there are two phases, a solid $\gamma = s$ and a fluid phase $\gamma = f$, volume average can be established in both regions. Also,

$$\phi^s = \Delta V_s/\Delta V = 1 - \Delta V_f/\Delta V = 1 - \phi^f \tag{4}$$

and for simplicity of notation one can drop the superscript f to get

$$\phi^s = 1 - \phi \tag{5}$$

As such, calling the instantaneous local velocities for the solid and fluid phases, $\mathbf{u}_s$ and $\mathbf{u}$, respectively, one can obtain the average for the solid velocity, within the solid phase, as follows,

$$\langle \mathbf{u} \rangle^s = \frac{1}{\Delta V_s} \int_{\Delta V_s} \mathbf{u}_s \, dV_s \tag{6}$$

with, in turn, can be related to an average velocity referent to the entire REV as,

$$\mathbf{u}_S = \overbrace{\frac{\Delta V_s}{\Delta V}}^{(1-\phi)} \underbrace{\frac{1}{\Delta V_s} \int_{\Delta V_s} \mathbf{u}_s \, dV_s \langle \mathbf{u} \rangle^s}_{\langle \phi \rangle^s} \tag{7}$$

A further approximation herein is that the porous bed is kept rigid and moves with a steady average velocity $\mathbf{u}_s$.

Both velocities can then be written as,

$$\mathbf{u}_D = \phi \langle \mathbf{u} \rangle^i \text{ and } \mathbf{u}_s = (1 - \phi) \langle \mathbf{u} \rangle^s = const \tag{8}$$

A relative velocity is then defined as,

$$\mathbf{u}_{rel} = \mathbf{u}_D - \mathbf{u}_S \tag{9}$$

Assuming that the relative movement between the two phases is macroscopically described by Eq. (9), the momentum equation reads,

$$\rho \left[\frac{\partial \mathbf{u}_D}{\partial t} + \nabla \cdot \left(\frac{\mathbf{u}_D \mathbf{u}_D}{\phi} \right) \right] = -\nabla (\phi \langle \bar{p} \rangle^i) + \mu \nabla^2 \mathbf{u}_D - \underbrace{\left[\frac{\mu \phi}{K} \mathbf{u}_{rel} + \frac{c_F \phi \rho |\mathbf{u}_{rel}| \mathbf{u}_{rel}}{\sqrt{K}} \right]}_{relative\ drag}, \tag{10}$$

TWO-ENERGY EQUATION MODEL

As for the flow, the macroscopic equations to heat transport in porous media are obtained by applying the average volume to microscopic equations. The mathematical model used to describe the heat transfer between the solid and fluid in a unit of a moving bed is based on the two-energy equations model, which can be written as follows.

$$\begin{aligned} \left\{ (\rho c_p)_f \phi \right\} \frac{\partial \langle T_f \rangle^i}{\partial t} + (\rho c_p)_f \nabla \cdot \left(\mathbf{u}_D \langle T_f \rangle^i \right) = \nabla \cdot \left\{ \mathbf{K}_{eff,f} \cdot \nabla \langle T_f \rangle^i \right\} \\ + h_i a_i \left(\langle T_s \rangle^i - \langle T_f \rangle^i \right) \end{aligned} \tag{11}$$

$$\left\{(1-\phi)(\rho\, c_p)_s\right\}\frac{\partial\langle T_s\rangle^i}{\partial\, t}+(\rho\, c_p)_s\,\nabla\cdot\left(\mathbf{u}_S\langle T_s\rangle^i\right)=\nabla\cdot\left\{\mathbf{K}_{eff,s}\cdot\nabla\langle T_s\rangle^i\right\}-h_i a_i\left(\langle T_s\rangle^i-\langle T_f\rangle^i\right) \tag{12}$$

where $\mathbf{K}_{eff,f}$ and $\mathbf{K}_{eff,s}$ are the effective conductivity tensors for fluid and solid, respectively, given by

$$\mathbf{K}_{eff,\,f}=[\phi\, k_f]\,\mathbf{I}+\mathbf{K}_{f,\,s}+\mathbf{K}_{disp} \tag{13}$$

$$\mathbf{K}_{eff,\,s}=[(1-\phi)\, k_s]\,\mathbf{I}+\mathbf{K}_{s,f} \tag{14}$$

where $\mathbf{I}$ is the unit tensor and $\mathbf{K}_{disp}$, $\mathbf{K}_{f,\,s}$, and $\mathbf{K}_{s,\,f}$ are tensors defined as

$$\text{Thermal dispersion}: -(\rho\, c_p)_f\,(\phi\ \langle{}^i\mathbf{u}^i T_f\rangle^i\ )=\mathbf{K}_{disp}\cdot\nabla\langle T_f\rangle^i \tag{15}$$

$$\text{Local conduction}:\begin{cases}\nabla\cdot\left[\frac{1}{\Delta V}\int\limits_{A_i}\mathbf{n}_i\, k_f T_f\, dA\right]=\mathbf{K}_{f,\,s}\cdot\nabla\langle T_s\rangle^i\\ -\nabla\cdot\left[\frac{1}{\Delta V}\int\limits_{A_i}\mathbf{n}_i\, k_s T_s\, dA\right]=\mathbf{K}_{s,f}\cdot\nabla\langle T_f\rangle^i\end{cases} \tag{16}$$

where $\mathbf{n}_i$ in Eq. (16), as already noted, is the unit vector pointing outwards of the fluid phase. In this work, for simplicity, one assumes that the overall thermal resistance between the two phases is controlled by the interfacial film coefficient rather than by the thermal resistance within each phase. As such, the local conduction coefficients $\mathbf{K}_{f,s}$, $\mathbf{K}_{s,f}$ are neglected here for the sake of simplicity. Additional information on the models in Eqs. (13) and (14) can be found in reference [25].

INTERFACIAL HEAT TRANSFER COEFFICIENT

The heat transferred between the two phases was modeled by means of a film coefficient h_i, or interstitial heat transfer coefficient, present in Eq. (11) and Eq. (12), such that,

$$h_i a_i\left(\langle T_s\rangle^i-\langle T_f\rangle^i\right)=\frac{1}{\nabla V}\int_{A_i}\mathbf{n}_i\cdot k_f\nabla T_f dA=\frac{1}{\Delta V}\int_{A_i}\mathbf{n}_i\cdot k_s\nabla T_s\, dA \tag{17}$$

where A_i is the interfacial area between the two phases and a_i is the interfacial area per unit volume or $a_i = A_i/\nabla V$. The high values of a_i make them attractive for transferring thermal energy via conduction through the solid followed by convection to a fluid stream.

Wakao et al. (1979) [26] obtained a heuristic correlation for a closely packed bed of particle diameter D and compared their results with experimental data. This

correlation for the interfacial heat transfer coefficient is given by,

$$\frac{h_i D}{k_f} = 2 + 1.1 Re_D^{0.6} Pr^{1/3}, \quad \text{for } \phi > 0.9 \tag{18}$$

Further, a numerical correlation for the interfacial convective heat transfer coefficient was proposed by Kuwahara et al. (2001) [27] for a laminar flow as,

$$\frac{h_i D}{k_f} = \left(1 + \frac{4(1-\phi)}{\phi}\right) + \frac{1}{2}(1-\phi)^{1/2} Re_D Pr^{1/3}, \text{valid for } 0.2 < \phi < 0.9. \tag{19}$$

Results in Eq. (19) depend on the porosity and are valid for packed beds of particle diameter D. In addition, Saito and de Lemos (2005) [28] also obtained the interfacial heat transfer coefficient for laminar flows though an infinite square rod array using the same methodology as Kuwahara et al. (2001) [27]. It is interesting to note that the interstitial correlations (18) and (19) for h_i do not take into consideration the solid phase thermal conductivity. Accordingly, transport of heat by conduction through the solid matrix is accounted for by the solid conductivity tensor, equation (14), which yields the conduction transport term in (12). Further, both correlations (18) and (19) have been used in a number of works for analyzing the transfer of energy between the solid matrix and the working fluid in saturated porous media [27, 28].

The interstitial heat transfer coefficient h_i is calculated by correlations Eq. (19) for laminar flow. However, since the relative movement between phases is seen as the promoter of convective heat transport from the fluid to the solid, or vice-versa, a relative Reynolds number defined as

$$Re_D = \frac{\rho |\mathbf{u}_{rel}| D}{\mu} \tag{20}$$

is used in correlation Eq. (19) instead of a Reynolds number based on the absolute velocity of the fluid phase. Accordingly, when the solid phase velocity approaches the fluid velocity, the only mechanism for transferring heat between phases is conduction.

NUMERICAL METHOD AND BOUNDARY CONDITIONS

The problem under investigation is laminar flow through a channel completely filled with a moving porous medium. The two cases considered here are depicted in Figure 1*b* and 1*c*, and the only difference between them is the reversal in the x-direction of the boundary conditions applied for both velocities at their entrances. The sole reason for considering two such possibilities was to guarantee computer accuracy when comparing the solutions obtained with the two cases, which should present a perfect mirror image with respect to each other.

The numerical method used to discretize the flow and energy equations was the control volume approach. The SIMPLE method of Patankar [29] was used to handle

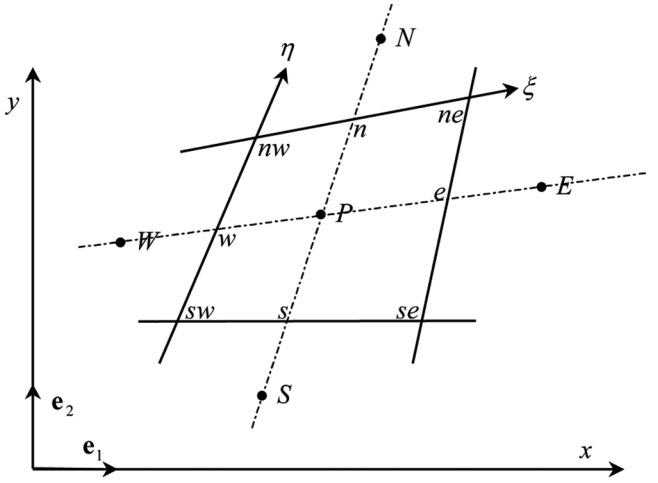

Figure 2. Control volume and notation.

the pressure-velocity coupling and was applied for relaxing the systems of algebraic equations.

Figure 2 presents a typical control volume written in the generalized coordinates system η–ξ. The discretized form of the two-dimensional conservation equation for a generic property φ, in permanent regime, is given by

$$I_e + I_w + I_n + I_s = S_\varphi \tag{21}$$

where I_e, I_w, I_n, and I_s represent, respectively, the fluxes of φ in the faces east, west, north, and south of the control volume and S_φ is its source term.

Standard source term linearization is accomplished by using

$$S_\varphi \approx S_\varphi^{**} \langle \varphi \rangle_p^i + S_\varphi^* \tag{22}$$

Discretization of the momentum equation in the x-direction gives,

$$S^{*x} = \left(S_e^{*x}\right)_P - \left(S_w^{*x}\right)_P + \left(S_n^{*x}\right)_P - \left(S_s^{*x}\right)_P + S_P^* \tag{23}$$

$$S^{**x} = S_\varphi^{**} \tag{24}$$

where, S^{*x} is the diffusive part, here treated in an explicit form. The second term, S^{**x}, entails the additional drag forces due to the porous matrix, which are here treated explicitly.

Convergence was monitored in terms of the normalized residue, which was set to be lower than 10^{-9}.

Boundary conditions are given by:

$$\text{On solid walls, } \langle \mathbf{u} \rangle^i = 0, q_w = 0 \tag{25}$$

For the west and east faces, boundary conditions will depend on the direction of fluid and feed stream as depicted in Figure 1, as follows:

Case of Figure 1*b* – counterflow with fluid moving west to east:

On the west face:

$$\mathbf{u}_D = \mathbf{u}_{inlet}, \langle T_f \rangle^i = T_{f_{in}} \tag{26}$$

$$\langle T_s \rangle^i = T_{s_{out}} \approx T_{f_{in}} + \frac{\frac{\partial}{\partial x}\left(\left(\rho c_p\right)_f u_{inlet} \langle T_f \rangle^i - \phi k_f \frac{\partial \langle T_f \rangle^i}{\partial x} \right)\Big|_{x=0}}{h_i a_i} \tag{27}$$

$$\text{On east face: } \mathbf{u}_s = \mathbf{u}_{s_{in}}, \langle T_s \rangle^i = T_{s_{in}} \tag{28}$$

$$\langle T_f \rangle^i = T_{f_{out}} \approx T_{s_{in}} + \frac{\frac{\partial}{\partial x}\left(\left(\rho c_p\right)_s u_{s_{in}} \langle T_s \rangle^i - (1-\phi) k_s \frac{\partial \langle T_s \rangle^i}{\partial x}\Big|_{x=L} \right)}{h_i a_i} \tag{29}$$

Boundary conditions (27) and (29) come from applying the corresponding transport equations (11) and (12), in their steady-state form, at west and east faces, respectively.

Case of Figure 1*c* – counterflow with fluid moving east to west:

On the west face

$$\mathbf{u}_s = \mathbf{u}_{s_{in}}, \langle T_s \rangle^i = T_{s_{in}} \tag{30}$$

$$\langle T_f \rangle^i = T_{f_{out}} \approx T_{s_{in}} + \frac{\frac{\partial}{\partial x}\left(\left(\rho c_p\right)_s u_{s_{in}} \langle T_s \rangle^i - (1-\phi) k_s \frac{\partial \langle T_s \rangle^i}{\partial x} \right)\Big|_{x=0}}{h_i a_i} \tag{31}$$

On the east face

$$\mathbf{u}_D = \mathbf{u}_{inlet}, \langle T_f \rangle^i = T_{f_{in}} \tag{32}$$

$$\langle T_s \rangle^i = T_{s_{out}} \approx T_{f_{in}} + \frac{\frac{\partial}{\partial x}\left(\left(\rho c_p\right)_f u_{inlet} \langle T_f \rangle^i - \phi k_f \frac{\partial \langle T_f \rangle^i}{\partial x} \right)\Big|_{x=L}}{h_i a_i} \tag{33}$$

It is interesting to note the practical application of the inlet boundary conditions. Real world engineering flows in actual reactors will most likely present a temperature distribution when the incoming flow, of either phase, is not well-insulated. However, when the feed stream is thermally isolated and the working fluid is well mixed and evenly distributed before entering the reactor, the use of constant temperature values at inlet may well represent the basic features of flow and heat transfer in such equipment. Examples of similar boundary conditions assuming constant values at inlet for moving beds are found in reference [30].

RESULTS AND DISCUSSION

As previously mentioned, Figure 1*a* shows two possibilities for the relative movement of phases. Both phases can co-flow in the same direction, in a parallel arrangement, or have opposite directions in the so-called counterflow configuration. Here, only counterflow cases are investigated. For the sake of checking the computer code accuracy, two equivalent cases are investigated. In the first case, the solid matrix moves from east to west, whereas the fluid enters through the west side of the porous reactor (Figure 1*b*). In an equivalent but reversed configuration, both solid and fluid exchange their side of entrance (Figure 1*c*).

Further, the channel shown in Figure 1 has length and height given by L and H, respectively. The porous matrix moves with constant velocity $\mathbf{u}_s$ in the opposite direction of the fluid velocity $\mathbf{u}_D$ (see Figure 1*a*). In the following figures, axial temperature profiles for both phases are presented for the two cases in Figures 1*b* and *1c*, with the sole purpose to show that results will be consistent with application of reserved boundary conditions.

The fluid and solid phases are given different temperatures at the inlet and non-dimensional temperatures for the solid and fluid are defined as:

$$\theta_{s,f} = \frac{\langle T_{s,f} \rangle^i - T_{\min}}{T_{\max} - T_{\min}} \tag{34}$$

where the subscripts s, f stands for the solid and fluid phases, respectively, and "max" and "min" refers to maximum and minimum temperatures of both phases. Also, it is interesting to mention that correctness of the energy balance of both phases was checked for every run to be presented, or say, heat leaving one phase was properly absorbed by the other. Comparisons with experimental data, however, are here not presented due to lack of experimental values in the literature, at least for the specific configurations here analyzed. Results herein should then be regarded as a first approximation subjected to refinement as more experimental data is made available in the literature.

EFFECT OF REYNOLDS NUMBER, Re_D

Figure 3 shows values for the longitudinal non-dimensional temperature profiles as a function of Re_D. The Reynolds number was calculated based on the relative velocity $\mathbf{u}_{rel}$, as given by equation (20), and for a fixed value $u_S/u_D = -0.5$. Figure 3 indicates that the cold fluid is heated up as it permeates the hot porous structure, which moves in the opposite direction of the fluid. It is observed that the higher the relative Reynolds number, resulting from increasing the opposing mass flow rates of both the fluid and the solid, with consequent increase on the relative velocity between the phases, more energy is convected into the system increasing the temperature difference between the phases along the channel. Although an increase in Re_D reflects in an increase in h_i, Eq. (19), resulting in a stronger interstitial heat exchange, the imposed elevation of both mass flow rates in order to keep $u_S/u_D = -0.5$ will result in larger temperature differences for the same length of the reactor. The corresponding effect is seen in Figure 3*b* when both flows have their directions reversed.

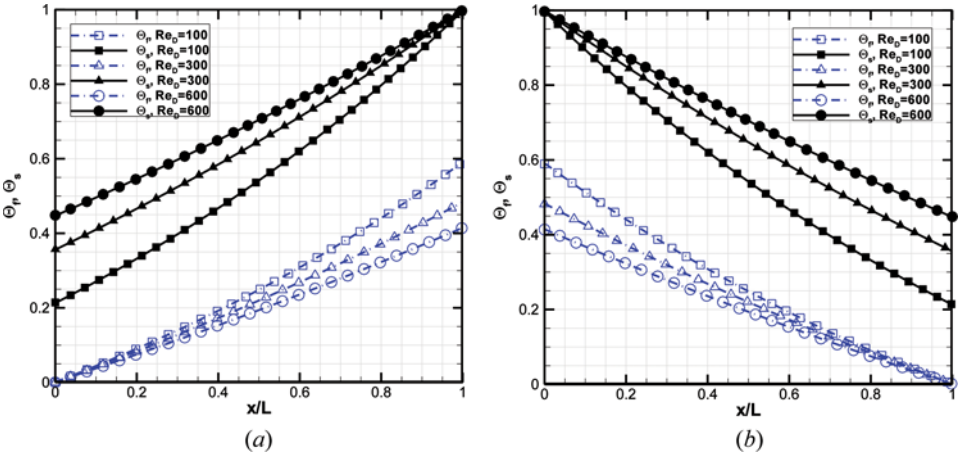

Figure 3. Nondimensional temperatures as a function of Re_D for $u_S/u_D = -0.5$, $k_s/k_f = 25$, $\mathrm{Da} = 3.371 \times 10^{-3}$, $\phi = 0.9$, and $(\rho c_p)_s/(\rho c_p)_f = 1.5$. (*a*) Flow moving west to east and (*b*) flow moving east to west (color figure available online).

EFFECT OF SLIP RATIO, u_S/u_D

Figure 4 shows temperature profiles for a moving bed as a function of u_S/u_D. In the plots shown in the figure, the fluid speed was kept constant in one direction ($Re_H = 1139$) and the solid speed, in the opposite direction, was varied leading to the increase of absolute values of u_S/u_D. It is observed that for higher absolute values of u_S/u_D, or higher relative velocities $u_{rel} = u_D - u_S$, the heating of the fluid is more efficient, raising its temperature at the fluid exit. The figure indicates that by increasing u_S/u_D, more thermal energy is brought into the system by the solid phase,

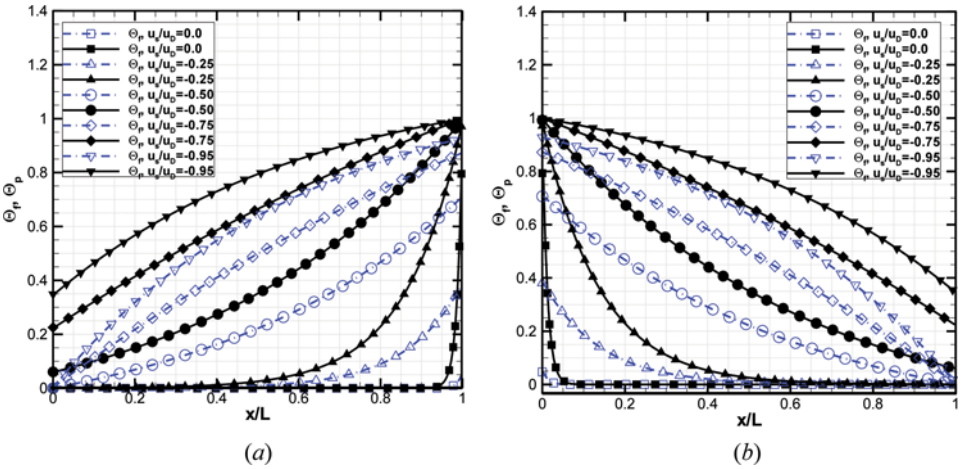

Figure 4. Nondimensional temperatures as a function of u_s/u_D, $\mathrm{Re}_H = 1139$, $k_s/k_f = 25$, $\phi = 0.9$, and $(\rho c_p)_s/(\rho c_p)_f = 1.5$. (*a*) flow moving west to east and (*b*) flow moving east to west (color figure available online).

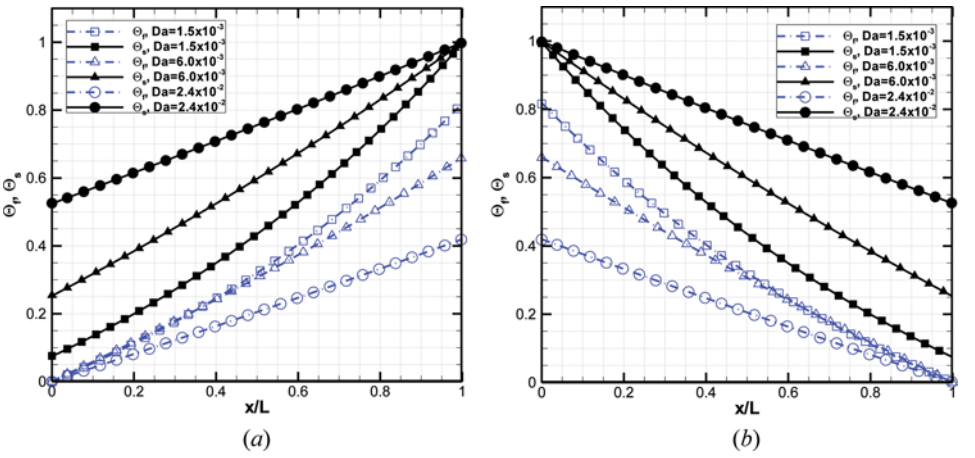

Figure 5. Nondimensional temperatures as a function of Da, $u_s/u_D = -0.5$, $k_s/k_f = 25$, $\phi = 0.9$, $\mathrm{Re}_D = 794$, and $(\rho c_p)_s/(\rho c_p)_f = 1.5$. (*a*) Flow moving west to east and (*b*) flow moving east to west (color figure available online).

leading to an increase in the solid temperature at a certain axial position x/L. Due to a greater Re_D, which is based on u_{rel}, better interstitial heat transfer is obtained, raising the fluid temperature at the same axial location. In all cases, it is observed that the outlet temperature of the fluid is greater than the outlet temperature of the solid.

EFFECT OF DARCY NUMBER, Da

Figure 5 shows the effect of the Darcy number $\mathrm{Da} = K/H^2$ on the axial temperature profiles. The decrease of the Darcy number is a consequence of decreasing the medium permeability, which is here computed by $K = D^2\phi^2/144(1-\phi)^2$, D being the associated particle diameter of the bed and ϕ its porosity. A reduction in K means an increase in flow resistance. For the simulations in the figure, the Reynolds number and the porosity were kept constant for all curves. It is observed in Figure 5 that for a small permeability, or small $\mathrm{Da} = K/H^2$ as a result of a decrease of particle diameter while keeping the porosity constant, a larger interfacial heat transfer area promotes energy transfer along the channel, resulting in a more efficient heat exchange between phases. This can be observed for $\mathrm{Da} = 1.5 \times 10^{-3}$ and for $\mathrm{Da} = 6 \times 10^{-3}$, where the outlet temperature of the fluid is greater than the outlet temperature of the solid.

EFFECT OF POROSITY, ϕ

Figure 6 shows the effect of porosity on the longitudinal temperature distribution. The Reynolds number, the velocity ratio u_S/u_D, the Darcy number, and the ratio of thermal capacity were kept constant for all curves. The figure indicates that for low porosities, a better exchange of heat is obtained between phases. For a

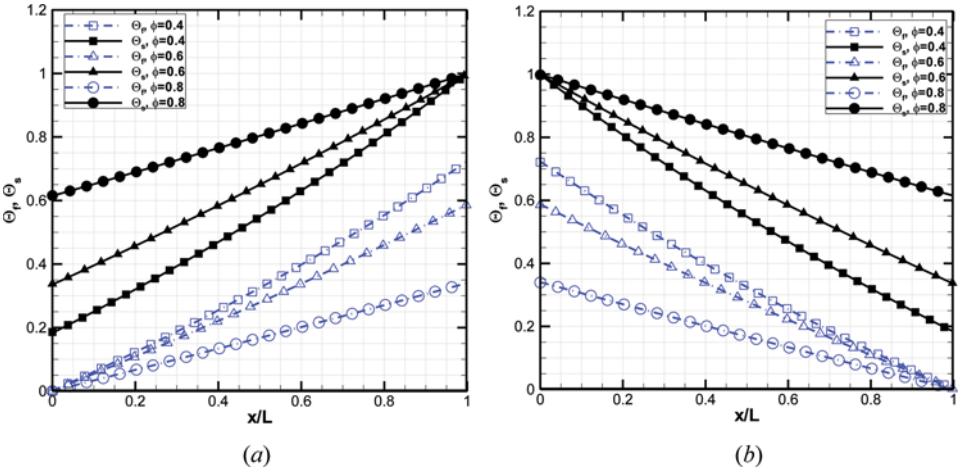

Figure 6. Nondimensional temperatures as a function of ϕ, $u_s/u_D = -0.5$, $(\rho c_p)_s/(\rho c_p)_f = 1.5$, $\mathrm{Da} = 0.1498$, and $\mathrm{Re}_D = 794$. (*a*) Flow moving west to east and (*b*) flow moving east to west (color figure available online).

fixed Reynolds number, a decrease in porosity corresponds to an increase on the interfacial heat transfer coefficient h_i Eq. (19). Consequently, the product $h_i a_i$ will increase as porosity ϕ decreases, enhancing the ability of the solid phase to heat up the colder fluid. Moreover, the lower the porosity, i.e., the greater the amount of solid material per total volume, the closer the fluid temperature will be to that of the solid temperature along the channel, which is caused by a greater exchange of heat between phases. This can be observed for $\phi = 0.4$ and for $\phi = 0.6$, where, in both

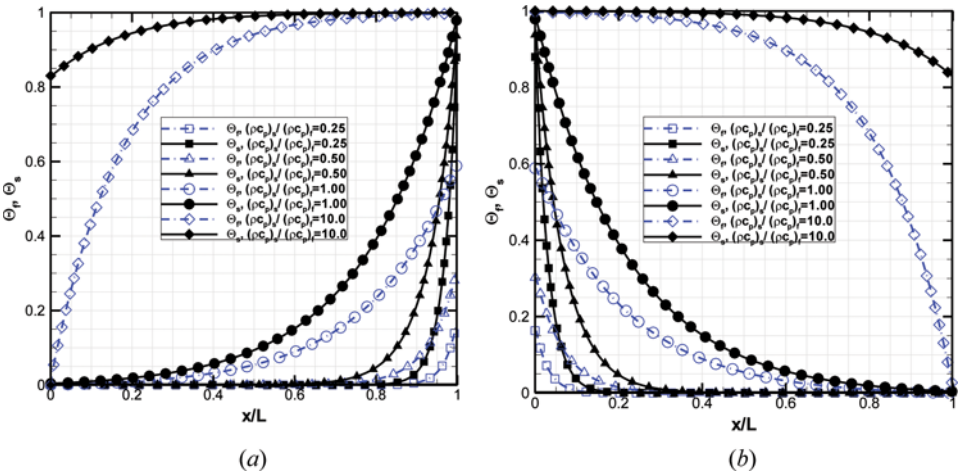

Figure 7. Nondimensional temperatures as a function of $(\rho c_p)_s/(\rho c_p)_f$, $u_s/u_D = -0.5$, $k_s/k_f = 25$, $\phi = 0.9$, $\mathrm{Da} = 1.498 \times 10^{-3}$, and $\mathrm{Re}_D = 794$. (*a*) Flow moving west to east and (*b*) flow moving east to west (color figure available online).

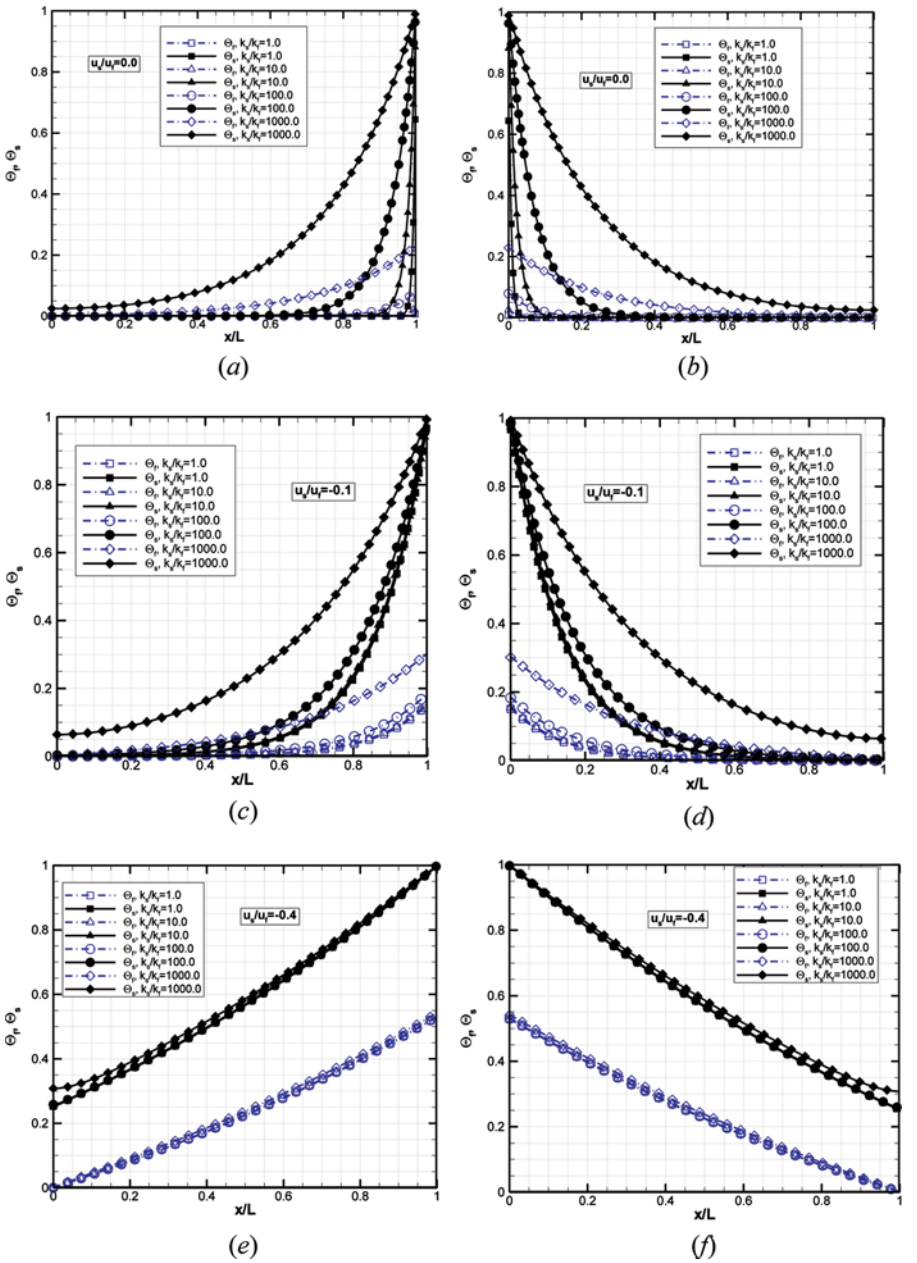

Figure 8. Nondimensional temperatures as a function of k_s/k_f, $\phi = 0.6$, $\mathrm{Da} = 4.162 \times 10^{-3}$, and $(\rho c_p)_s/(\rho c_p)_f = 1.5$. (*a*) Flow moving west to east and (*b*) flow moving east to west (color figure available online).

cases, the outlet fluid temperature is greater than that of the solid temperature at exit.

EFFECT OF THERMAL CAPACITY RATIO $(\rho c_p)_s/(\rho c_p)_f$

The effect of the thermal capacity ratio on dimensionless temperatures is shown in Figure 7. The density and specific heat of the fluid are kept constant and given by $\rho_f = 0.4345\, kg/m^3$ and $c_{p_f} = 1986.8$ J/kg K, respectively. It is observed in the figure that when the heat capacity of the solid is greater than that of the fluid, the solid temperature presents less variation in temperature across the reactor. When the thermal capacity of the solid $(\rho c_p)_s$ is high, more energy exchange is needed to vary the temperature of the solid by a certain amount. Also, for all cases, the outlet fluid temperature is greater than the value of the solid temperature at the exit. For the highest ratio analyzed, $(\rho c_p)_s/(\rho c_p)_f = 10.0$, the solid temperature undergoes the least variation, as expected.

EFFECT OF THERMAL CONDUCTIVITY RATIO k_s/k_f

Finally, Figure 8 show the effect of k_s/k_f on longitudinal non-dimensional temperatures for distinct velocity ratios u_S/u_D. For a fixed solid substrate, $u_s/u_D = 0$ (Figure 8*a,b*), one note that the higher the ratio k_s/k_f, the stronger is the axial conduction through the solid, raising its temperature and, consequently, heating up the fluid at the outlet (see cases in Figure 1*b* and *c* for data in Figure 8*b* and *a*, respectively).

With the slow movement of the solid bed, $u_s/u_D = -0.1$, Figure 8*c* and *d* show that the solid temperature is raised not only by axial conduction along the bed, but also due to increase of the fluid temperature due to a better exchange of heat between phases, an effect caused by increase of the interfacial heat transfer coefficient h_i, which, in turn, is a result of increasing the relative velocity and, consequently, Re_D (see Eq. (19)). As a result, values of both the fluid and the solid temperatures along the channel increase with increase of k_s/k_f. Compared to the previous case for $u_s/u_D = 0$, the effect of k_s/k_f now seems to be of a lesser importance since inter-phase heat transport starts to play a role in temperature distributions as the solid velocity increases. Such conclusion becomes more evident for $u_s/u_D = -0.4$ (Figure 8*e,f*), when the ratio of thermal conductivity causes little influence on the temperature distribution within each phase along the channel. For high solid mass flow rates, with absolute values of u_s/u_D approaching 1, there is a better heat exchange between the phases along the channel, regardless of the value of the thermal conductivity of the solid.

CONCLUSIONS

This article investigated the behavior of a two-energy equation model to simulate flow and heat transfer in a counterflow porous moving bed. Numerical solutions for laminar flow were obtained for distinct values of Reynolds number Re_D, slip

ratio u_S/u_D, Darcy number Da, porosity ϕ, ratio of thermal capacity $(\rho c_p)_s/(\rho c_p)_f$, and ratio of thermal conductivity k_s/k_f.

It is observed, according to the results obtained, that an exchange of heat between phases is more efficient when compared with parallel flow cases. Movement of the solid material contrary to the direction of the fluid, with higher Re_D or slip ratio u_S/u_D, enhances heat transfer between phases. The same effect was observed for smaller Da, smaller ϕ, and higher $(\rho c_p)_s/(\rho c_p)_f$ and k_s/k_f.

REFERENCES

1. M. Vera and A. Liñán, Laminar Counterflow Parallel-Plate Heat Exchangers: Exact and Approximate Solutions, *Int. J. of Heat and Mass Transfer*, vol. 54, pp. 490–499, 2010.
2. M. Vera and A. Liñán, Exact Solution for the Conjugate Fluid–Fluid Problem in the Thermal Entrance Region of Laminar Counterflow Heat Exchangers, *Int. J. of Heat and Mass Transfer*, vol. 54, pp. 490–499, 2011.
3. N. Ghorbani, H. Taherian, M. Gorji, and H. Mirgolbabaei, An Experimental Study of Thermal Performance of Shell-and-Coil Heat Exchangers, *Int. Comm. in Heat and Mass Transfer*, vol. 37, pp. 775–781, 2010.
4. F. P. Incropera, F. P. DeWitt, and D. P. *Introduction to Heat Transfer*, 3rd ed., Wyley, New York, 1996.
5. M. R. Ansari and V. Mortazavi, Simulation of Dynamical Response of a Countercurrent Heat Exchanger to Inlet Temperature or Mass Flow Rate Change, *Appl. Thermal Eng.*, vol. 26, pp. 2401–2408, 2006.
6. S. C. Kranc, Performance of Counterflow Cooling Towers with Structured Packings and Maldistributed Water Flow, *Numerical Heat Transfer, Part A: Applications*, vol. 23, pp. 115–127, 1993.
7. H. Ay, R. R. Johnson, Yang, Wen-Jei, Direct-Contact Heat Transfer Between a Rising Dispersed Phase in a Counterflow Stream, *Numerical Heat Transfer, Part A: Applications*, vol. 26, pp. 667–682, 1994.
8. N. Souid and A. Bontemps, Countercurrent Gas-Liquid Flow in Plate-Fin Heat Exchangers with Plain and Perforated Fins, *Int. J. of Heat and Fluid Flow*, vol. 22, pp. 450–459, 2001.
9. K. S. Rajan, S. N. Srivastava, B. Pitchumani and B. Mohanty, Simulation of Countercurrent Gas–Solid Heat Exchanger: Effect of Solid Loading Ratio and Particle Size, *Appl. Thermal Eng.*, vol. 27, pp. 1345–1351, 2007.
10. M. S. Valipour and Y. Saboohi, Numerical Investigation of Nonisothermal Reduction Hematite Using Syngas: The Shaft Scale Study, *Modeling Simul. Mater. Sci. Eng.*, Vol. 15, pp. 487–507, 2007.
11. R. Henda and D. J. Falcioni, Modeling of Heat Transfer in a Moving Packed Bed: Case of The Preheater In Nickel Carbonyl Process, *Journal of Applied Mechanics – ASME*, Vol. 73, no. 1, pp. 47–53, 2006.
12. C. Ryu Y. B. Yang, A. Khor, N. E. Yates, V. N. Sharifi and J. Swithenbank, Effect of Fuel Properties on Biomass Combustion: Part I. Experiments—Fuel Type, *Equivalence Ratio and Particle Size, Fuel*, vol. 85, pp. 1039–1046, 2006.
13. C. Boman, A. Nordin and L. Thaning, Effects of Increased Biomass Pellet Combustion on Ambient Air Quality in Residential Areas – A Parametric Dispersion Modeling Study, *Biomass and Bioenergy*, vol. 24, pp. 465–474, 2003.
14. T. Shimizu, J. Han, S. Choi, L. Kim and H. Kim, Fluidized-Bed Combustion Characteristics of Cedar Pellets by Using an Alternative Bed Material, *Energy & Fuels*, vol. 20, pp. 2737–2742, 2006.

15. T. K. Kayal and M. Chakravarty, Mathematical Modeling of Continuous Updraft Gasification of Bundled Jute Stick – A Low Ash Content Woody Biomass, *Bioresource Technology*, vol. 49, no. 1, pp. 61–73, 1994.
16. A. Rogel, and J. Aguillón, The 2-D Eulerian Approach of Entrained Flow, and Temperature in a Biomass Stratified Downdraft Gasifier, *Amer. J. of Appl. Sci.*, Vol. 3, no. 10, pp. 2068–2075, 2006.
17. T. Nussbaumer, Combustion and Co-Combustion of Biomass: Fundamentals, Tecnologies, and Primary Measures for Emission Reduction, *Energy & Fuels*, vol. 17, pp. 1510–1521, 2003.
18. A. C. Pivem and M. J. S. de Lemos, Laminar Heat Transfer in a Moving Porous Bed Reactor Simulated with a Macroscopic Two – Energy Equation Model, vol. 55, nos. 7–8, pp. 1922–1930, 2012.
19. M. B. Saito and M. J. S. de Lemos, Interfacial Heat Transfer Coefficient for Non-Equilibrium Convective Transport in Porous Media, *Int. Comm. in Heat And Mass Transfer*, vol. 32, no. 5, pp. 666–676, 2005.
20. M. J. S. de Lemos and M. B. Saito, Computation of Turbulent Heat Transfer in a Moving Porous Bed using a Macroscopic Two-Energy Equation Model, *Int. Comm. in Heat and Mass Transfer*, vol. 35, pp. 1262–1266, 2008.
21. M. J. S. de Lemos, Turbulence in Porous Media: Modeling and Applications, *Elsevier, Amsterdam*, 2006.
22. E. J. Braga and M. J. S. de Lemos, Laminar Natural Convection in Cavities Filled with Circular, and Square Rods, *Int. Comm. Heat Mass Transfer*, vol. 32 no. 10, pp. 1289–1297, 2005.
23. W. G. Gray, and P. C. Y. Lee, On the Theorems for Local Volume Averaging of Multiphase System, *Int. J. of Multiphase Flow*, vol. 3, pp. 333–340 1977.
24. S. Whitaker, Advances in Theory of Fluid Motion in Porous Media, *Indust. Eng. Chem.*, vol. 61, pp. 14–28, 1969.
25. M. B. Saito and M. J. S. de Lemos, A Correlation for Interfacial Heat Transfer Coefficient for Turbulent Flow Over an Array of Square Rods, *J. Heat Transfer*, vol. 128, pp. 444–452, 2006.
26. N. Wakao, S. Kaguei and T. Funazkri, Effect of Fluid Dispersion Coefficients on Particle-Fluid Heat Transfer Coefficient in Packed Bed, *Chem. Eng. Sci.*, vol. 34, pp. 325–336, 1979.
27. F. Kuwahara, M. Shirota and A. Nakayama, A Numerical Study of Interfacial Convective Heat Transfer Coefficient in Two-Energy Equation Model for Convection in Porous Media, *Int. J. Heat Mass Transfer*, vol. 44, pp. 1153–1159, 2001.
28. M. B. Saito, M. J. S. de Lemos, Interfacial Heat Transfer Coefficient for Non-Equilibrium Convective Transport in Porous Media, *Int. Comm. of Heat and Mass Transfer*, vol. 32, no. 5, pp. 666–676, 2005.
29. S. V. Patankar, *Numerical Heat Transfer and Fluid Flow*, Hemisphere, Washington, DC, 1980.
30. H. Guoxin, X. Wei and L. Yaqin, Heat Transfer and Gas Flow through Feed Stream within Horizontal Pipe, *Transport in Porous Media*, vol. 52, pp. 371–387, 2003.